AD-A271 129

)CUMENTATION PAGE

Form Approved
OMB No 0704-0188

2. REPORT DATE	3. REPORT TYPE AND DATES COVERED
22 June 1993	Final Report, 1 - 14 May 93

4. TITLE AND SUBTITLE
High Performance Heavy Alloys by Alloying & Process Control

5. FUNDING NUMBERS
2

6. AUTHOR(S)
A. Belhadjhamida and R. M. German

7. PERFORMING ORGANIZATION NAME(S) AND ADDRESS(ES)
P/M Lab, Penn State University
118 Research Building West
University Park, PA 16802-6809

8. PERFORMING ORGANIZATION REPORT NUMBER

9. SPONSORING/MONITORING AGENCY NAME(S) AND ADDRESS(ES)
U.S. Army Research Office
P. O. Box 12211
Research Triangle Park, NC 27709-2211

10. SPONSORING/MONITORING AGENCY REPORT NUMBER
ARO 29326.14-MS

93-24941

11. SUPPLEMENTARY NOTES
The view, opinions and/or findings contained in this report are those of the author(s) and should not be construed as an official Department of the Army position, policy, or decision, unless so designated by other documentation.

12a. DISTRIBUTION/AVAILABILITY STATEMENT
Approved for public release; distribution unlimited.

12b. DISTRIBUTION CODE

13. ABSTRACT *(Maximum 200 words)*

The kinetics and processing conditions of liquid phase sintering (LPS) have been addressed in the development of a novel heavy alloy, W-Ni-Mn. Solubility criteria were considered in the selection of manganese as an alloying element to the W-Ni system. The addition of manganese resulted in a depressed melting point of the matrix and consequently sintering in this system was achieved at temperatures 300°C lower than in the conventional heavy alloys. Concurrent with solubility criteria, the rearrangement stage in liquid phase sintering was treated. When capillary and viscous drag forces are accounted for, the time scales in rearrangement were found to be in the microseconds range for metal systems. On the other hand, heat transfer was found to be the rearrangement time limiting factor for metallic specimens with time scales in the range of seconds. Further, depending on the green density and the system under consideration, there exists specific specimen dimensions where a transition from heat transfer to capillary control over the rearrangement time. These dimensions are, however, in the micrometer range.

14. SUBJECT TERMS	15. NUMBER OF PAGES
Tungsten heavy alloys, grain growth, alloying, mechanical properties, microprobe analysis	24
	16. PRICE CODE

17. SECURITY CLASSIFICATION OF REPORT	18. SECURITY CLASSIFICATION OF THIS PAGE	19. SECURITY CLASSIFICATION OF ABSTRACT	20. LIMITATION OF ABSTRACT
UNCLASSIFIED	UNCLASSIFIED	UNCLASSIFIED	UL

High Performance Heavy Alloys by Alloying and Process Control

Final Report

A. Belhadjhamida and R. M. German

June 22, 1993

U.S. Army Research Office
Post Office Box 12211
Research Triangle Park, NC 27709-2211

Grant Number DAAL03-91-G-0309

The Pennsylvania State University
P/M Lab, 118 Research West
University Park, PA 16802-6809

Approved for public release; distribution unlimited.

Table of Contents

List of Figures

List of Tables

Abstract

The kinetics and processing conditions of liquid phase sintering (LPS) have been addressed in the development of a novel heavy alloy, W-Ni-Mn. Solubility criteria were considered in the selection of manganese as an alloying element to the W-Ni system. The addition of manganese resulted in a depressed melting point of the matrix and consequently sintering in this system was achieved at temperatures 300°C lower than in the conventional heavy alloys. Concurrent with solubility criteria, the rearrangement stage in liquid phase sintering was treated. When capillary and viscous drag forces are accounted for, the time scales in rearrangement were found to be in the microseconds range for metal systems. On the other hand, heat transfer was found to be the rearrangement time limiting factor for metallic specimens with time scales in the range of seconds. Further, depending on the green density and the system under consideration, there exists specific specimen dimensions where a transition from heat transfer to capillary control over the rearrangement time. These dimensions are, however, in the micrometer range.

Coarsening in liquid phase sintered systems was also considered. A coalescence function was introduced to the continuity equation for the grain size distribution. At high volume fractions of the solid phase, the grain size distribution was skewed to the right as compared to the symmetrical behavior at low solid volume fractions. While these observations agree with previous experimental measurements on liquid phase sintered microstructures and the experimental measurements in the W-Ni-Mn system, the overall effect of coalescence on the grain size distribution functions is minimal. This is due to the fact that coarsening kinetics in coalescence follows the same time dependency as in diffusion.

In the processing of this new heavy alloy, variables such as the initial powder purity, the processing atmosphere, the sintering temperatures, and the nickel to manganese ratio were considered. For high densification, the oxygen content in the initial powders must be controlled. It is found that a 3/2 Ni to Mn ratio was optimum to avoid the high vapor pressure and oxidation of manganese while maintaining high mechanical properties. During tensile testing, the as-sintered specimens failed in the elastic region. A post-sintering heat treatment in argon followed by water quenching proved beneficial in this system. In fact, during cooling from the sintering temperature, the microstructure undergoes phase changes resulting in intermetallic compound formation in accordance with the Ni-Mn phase diagram. The additional heat treatment followed by quenching avoids intermetallic formation. The resulting average mechanical properties were 900 MPa ultimate tensile strength (UTS) and 10% ductility. When a milling treatment was applied to the initial powders, the UTS further increased to 980 MPa with no effect on the ductility for the 90W-6Ni-4Mn system sintered at 1200°C for 1 hour in a hydrogen atmosphere. These properties are comparable to the classical heavy alloys where sintering is usually performed at 1500°C with mechanical properties of 900 MPa and 30% ductility for the 90W-7Ni-3Fe composition.

Introduction

Tungsten heavy alloys (WHA) are two phase composites consisting of tungsten grains dispersed in a low melting temperature matrix. Due to their high density, high strength associated with the bcc tungsten phase, and high ductility attributed to the fcc matrix, these alloys are used in applications such as kinetic energy penetrators, radiation shielding, counterbalances, vibrational damping devices, and other military and civilian applications. Since tungsten has a high melting

point ~ 410°C), the sintering of tungsten heavy alloys usually occurs through liquid phase sintering. Ni-Fe, Ni-Co, Ni-Fe-Co, Ni-Cu, and Cu elemental powders are usually mixed with tungsten and the composite is sintered at temperatures where solid tungsten grains coexist with a liquid matrix. The presence of the liquid accelerates the densification kinetics relative to solid-state sintering. Four mechanisms are usually associated with liquid phase sintering; 1) solid-state sintering prior to liquid formation, 2) initial particle rearrangement due to capillary forces exerted by a wetting liquid, 3) prolonged solution-reprecipitaion associated with systems where the solid phase is soluble in the liquid, and 4) grain coarsening and final pore elimination [1-11].

Much understanding has been acquired in the arena of tungsten heavy alloys and most of the theoretical work in liquid phase sintering has been derived from experimental observations in tungsten heavy alloys. However, there are several discrepancies between theory and experiment. These discrepancies arise from the difficulties of relating the many variables involved in the densification and the microstructure evolution of these alloys, such as temperature, time, particle shape and size, homogeneity of the mixture of different alloying elements, processing conditions, and the overlap of the different mechanisms involved in the densification of these alloys, such as particle rearrangement, solution-reprecipitation, and grain growth.

In liquid phase sintered systems, the contribution of solid state sintering to LPS is usually ignored. In fact most of the modelling of LPS has focused on large scale particulate systems (100 μm). This results in practically negligible solid state shrinkage during heating. For example, a 90%W-7%Ni-3%Fe composition by weight densifies to 98% and 90% of theoretical for respectively 0.7 μm and 3.2 μm average tungsten particle size sintered at 1400°C for 1 hour. In the same time, the processing of these alloys through liquid phase sintering occurs at temperatures as high as 1520°C due to the high melting point of the nickel based matrix phase.

On one hand, nickel is beneficial in the densification of WHA. In fact tungsten has a high solubility in nickel which favors enhanced solution-reprecipitation. On the other hand, the high solubility of tungsten in the matrix results in accelerated grain growth and accordingly a coarse microstructure may result.

Therefore our attention has focused on matrices based on nickel with alloying additions that lower the liquid formation temperatures and limit the solubility of tungsten in the liquid phase. A low solubility of tungsten in the liquid phase is favorable, since it allows for a finer grain size which consequently yields high mechanical performance [12]. In addition, low sintering temperatures reduce the cost in processing of tungsten heavy alloys.

In the development of a new heavy alloy, solubility criteria between the alloying elements and tungsten need to be considered. In the first part of this work, the above criteria coupled with a theoretical treatment of the capillary induced rearrangement stage and grain growth are presented. This theoretical treatment provides a basis for understanding liquid phase sintering with respect to tungsten heavy alloys. We then proceed to the development of a new heavy alloy, W-Ni-Mn. The processing and the densification kinetics are emphasized. The microstructure evolution in this system is examined with respect to the processing conditions. The resulting properties of this new heavy alloy are then compared to the more traditional heavy alloys.

Theoretical Investigation

In searching for an alloying element for nickel, the following criteria were adopted;

1. complete solubility between nickel and the alloying element,
2. depressed melting point with the addition of the alloying element,
3. low solubility of tungsten in the alloying element,
4. low solubility of the alloying element in tungsten,
5. avoidance of intermetallic formation between W and the alloying element.

The depressed melting point on alloying nickel avoids sintering at high temperatures. A low solubility of tungsten in the alloying element is favorable to slow grain growth and allow for microstructural refinement; consequently, improved mechanical performance. The mechanical performance is degraded when an intermetallic forms between tungsten and the alloying elements, since the tungsten-matrix interface cohesion is lowered.

Figure 1 is a binary phase diagram of the nickel-manganese system [13]. As shown in this figure, liquid formation is achieved at temperatures as low as 1040°C for the 40wt% nickel and 60wt% manganese composition. Both nickel and manganese have complete solubility in each other. Unfortunately, the W-Mn phase diagram is not available in the literature. Nevertheless it is reported [90,91] that liquid Mn has no solubility for tungsten. This observation will be confirmed later using microprobe analysis. Therefore, it is expected that the addition of Mn to the W-Ni system will result in a refinement of the microstructure due to decreasing the solubility of tungsten in the matrix and possibly decreasing its diffusion coefficient [7,12].

The Ni-Mn binary phase diagram shows a large field of intermetallics of nickel and manganese. These intermetallics will not affect the sintering behavior in W-Ni-Mn, since the processing region of interest occurs at the onset of liquid formation. Further, nickel stabilizes gamma manganese (γ Mn) which has a FCC structure and is its most ductile phase. Aside from thermodynamic considerations, the selection of a new heavy alloy processed through LPS requires good wetting of the solid phase (tungsten) by the liquid phase. Wetting induces capillary forces that result in the approach, rearrangement of particles and consequently densification of the compact.

Rearrangement During Liquid Phase Sintering

Various investigators [14-18] have considered the rearrangement stage during liquid phase sintering. However, no effort was applied to compare the time scales involved in rearrangement with experimental observations. The purpose of this analysis is to find the time limiting factor for the rearrangement stage during liquid phase sintering. Previous experimental *in situ* observations of rearrangement [15,19,20] show that it takes from seconds to minutes for rearrangement processes in a loose powder packing. Further, within the whole process, instantaneous regrouping of particles occurred in clusters, but not uniformly throughout the compact. In the first part of this analysis, the capillary forces and the time scales involved in rearrangement shrinkage are treated, then the findings are compared with the time scales for heat transfer through a porous powder compact at the melting point of the matrix. In this method, a time limiting factor can be established.

In the case of two particles connected by a liquid bridge, capillary forces arise due to the surface tension of the liquid-vapor and the liquid-solid interfaces. A model geometry describing the above configuration was presented by Hwang and German [21] and is given in Figure 2. In this figure, θ is the contact angle between the liquid and the solid, R_L and R_S are the radii of the large and the small particles, α and β are the angles at which the solid-liquid-vapor phases intersect at points P_L and P_S for the large and small spherical particles, D is the interparticle separation distance, S and T are the two radii of curvature at any point on the liquid profile, where T is in a plane orthogonal to the X-Y plane containing S, and ϕ is the angle between the X-axis and the surface tension vector γ_{LV} . The capillary force between the two spheres is then calculated using the well known force equation [16,22];

$$F = \pi Y^2 P_{LV} + 2\pi Y \gamma_{LV} \cos(\phi) \qquad (1)$$

The first term in Equation 1 describes the pressure at any cross-section of the liquid perpendicular to the X-axis arising from the curvature of the liquid meniscus. The pressure term arising from the perimeter of contact of the liquid cross-section is given in the second term of Equation 1.

The above approach is extended to the shrinkage and swelling phenomena associated with the capillary effect. First the capillary forces as a function of the particle separation are calculated. Following the work of Fortees [17] and using Newton's second law, this force can then be expressed as;

$$F = M_r \frac{d^2D}{dt^2} \qquad (2)$$

In Equation 2, M_r is the reduced mass of the two particles (i.e. the sum of the two masses divided by 2) and D is the interparticle separation. In the work of Fortees, however, a circular approximation to the liquid profile was used, where the radius of curvature 1/S in Figure 2 is constant. This is not appropriate since the radius of curvature 1/T orthogonal to 1/S is not constant. Such an assumption results in a variation of the pressure P_{LV} along the liquid meniscus and therefore a distortion in its profile.

The next step consists of writing the viscous drag term as a function of the interparticle distance and time,

$$F_{drag} = \eta \dot{\epsilon} \zeta(X) = \eta \frac{dX}{Xdt} \zeta(X) \sim \eta \frac{dX}{X^2 dt} V_f \qquad (3)$$

Where η and V_f are the liquid viscosity and volume fraction and ζ is the cross sectional area at any distance X. In Equations 3, the liquid phase is assumed Newtonian. For the calculation of the capillary forces, Equation 1 is solved as a function of the interparticle distance. To calculate the times involved in the rearrangement processes, Equation 2 is equated to the capillary term (Equation 1) less the viscous drag term (Equation 3).

Figures 3 and 4 are plots of the dimension-less capillary force, $(F/(\gamma_{lv} R_S)$ where R_S is the radius of the small particle, as a function of the interparticle distance. As shown in these figures, aside from the contact angle, the particle size ratio (the radius of the large particle divided by the radius of the small particle, denoted C) and the liquid volume fraction (V_f) have

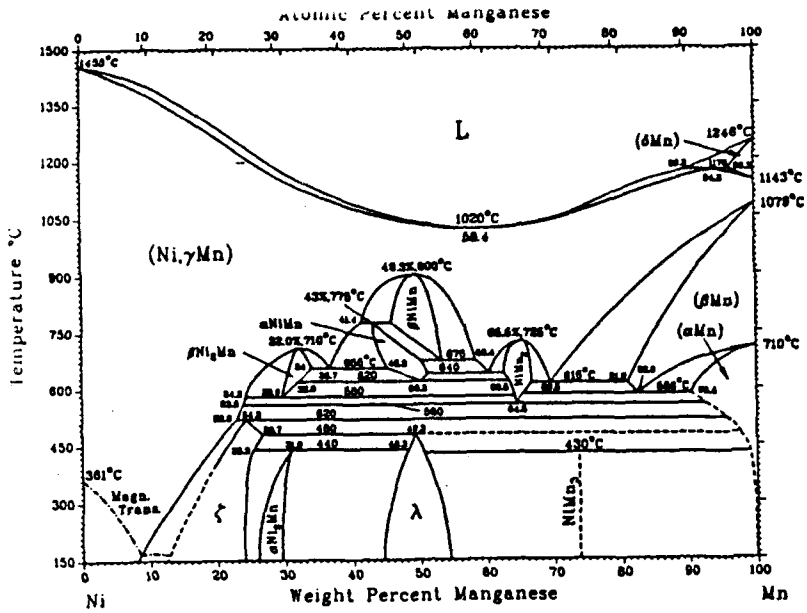

Figure 1. The Ni-Mn binary alloy phase diagram [13].

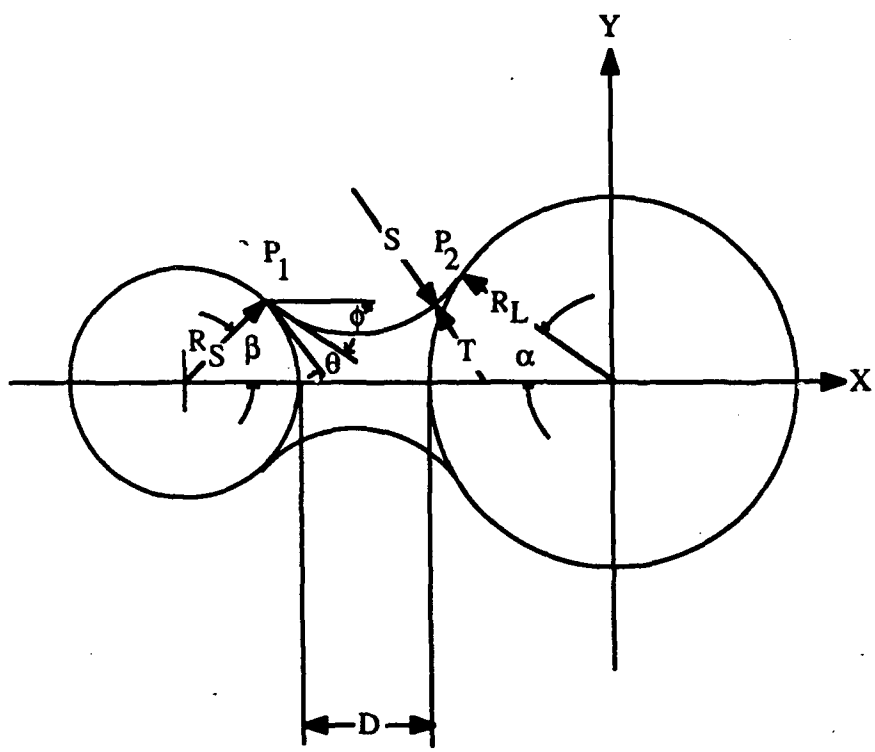

Figure 2. Model configuration of two particles connected by a liquid bridge [21].

a noticeable effect on the capillary force. In fact, as the size ratio increases, the normalized capillary force on the small particle increases. As a consequence, for a system where there is no solubility of the solid in the liquid, a broad particle size distribution would yield higher shrinkage than that of monosize particles. The effect of the volume fraction of liquid is also explored. From Figure 4, we can see that low liquid volumes promote higher capillary forces as also observed by Cahn and Heady [16]. Consequently a homogeneous distribution of the liquid phase between the solid phase can promote high densification due to capillary forces without the need for large volume fractions of liquid.

Since W-Ni-Mn data are not available for the time calculations, we will use W-Cu as an upper bound estimate since copper has a very high thermal conductivity. Using Equation 1-3 and data for W and Cu at the melting temperature of Cu. For all iterations involved in solving the differential equation 2, the times involved are on the order of microseconds. For a multiparticle system, we assume that the times over each pair of approaching particles are additive. For example, for a cube of 1 cm^3 volume consisting of a cubic close packing of particles, assuming that the particles are monosize and separated by liquid bridges of length 0.25 times the particle size, then the times for the rearrangement process to occur is 6.9 ms, and 29.1 μs for respectively 1 and 100μm tungsten particle sizes. In this calculation, we have added the times of approach of particles over half the diagonal of the cube, the contact angle is 8°, the volume fraction of the liquid phase is 0.1. The above findings do not agree with *in-situ* observations, with reported times in the range of seconds, suggesting that another phenomena is governing rearrangement for metal systems with respect to the time scales involved.

Since the times involved in the rearrangement stage do not agree with experimental observations, the thermal transport from the surface to the center of a composite structure is considered at the melting point of the matrix. The time difference for the center of the sphere to reach the surface temperature is;

$$\Delta t = \frac{1}{6}\tau_0, \quad \tau_0 = \frac{L^2}{k} \tag{4}$$

where L is the radius of the sphere and k is the thermal diffusivity. Using Equation 4, for W, Cu, and Fe the time differences are respectively 0.11, 0.05, and 0.85 s. However, the real problem at hand consists of calculating the times for heat transfer in a three phase specimen, the solid, liquid, and pore phases.

In the case of a loose powder or a powder compact, heat transfer at high temperatures is governed by conduction through the particle contacts, conduction in the pores due to the vapor phase (in the case of vacuum this is not valid), convection due to the gas in the pores, and radiation in the pores. The radiation effect has a major contribution at high temperatures and vacuum. In this analysis, only the effects of radiation and conduction on the thermal conductivity of the composite are considered, since the contribution of convection is only valid for large pore sizes (in the mm range). Luikov et al. [23] calculated the effective thermal conductivity for loose and compacted powders giving an expression depending on porosity, thermal conductivity of the solid and gas phases. Using the analysis of Luikov and equation 4, heat transfer times vary from 0.3 to 0.7 s and 1 to 3 s for the W-30Cu and Fe-Cu systems, as the porosity varies from 30 to 60%. In the above cases, the gas phase is hydrogen. When particle contacts are considered, especially in the case of loose powders, a lower bound for the effective thermal conductivity of

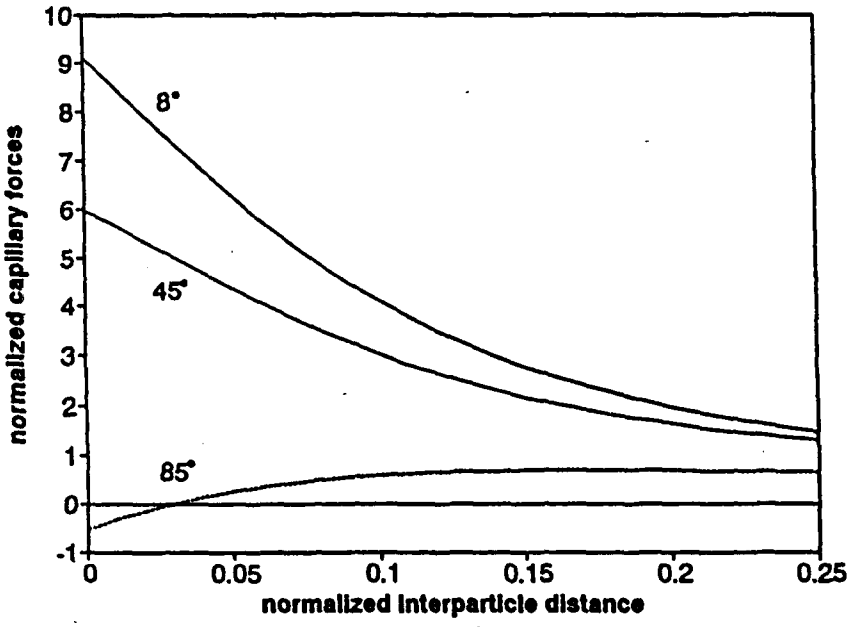

Figure 3. Capillary forces as a function of interparticle distance for a particle size ratio of 5, 0.01 volume fraction of liquid, and contact angles of 8, 45, and 85°.

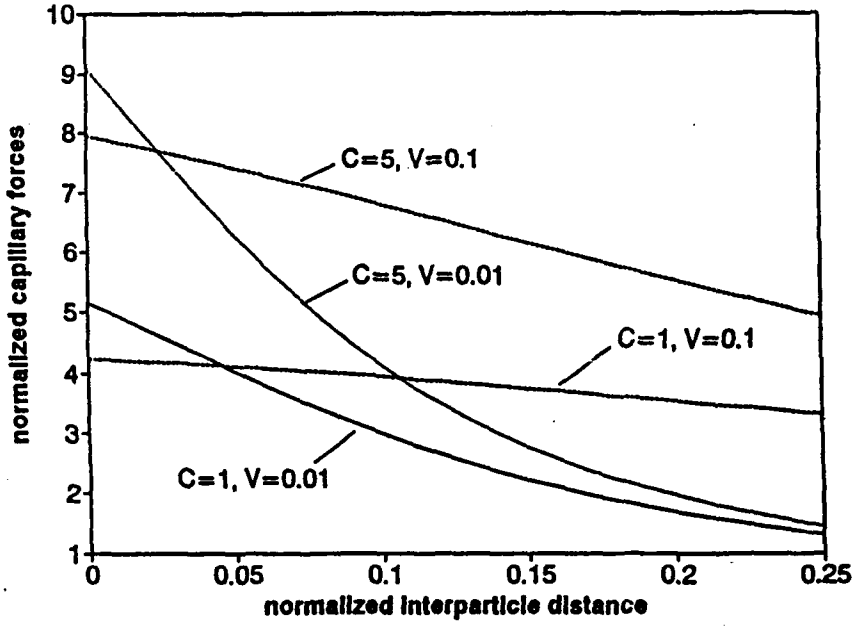

Figure 4. Capillary forces versus interparticle distance for an 8° contact angle configuration. (C is the particle size ratio and V_f is the liquid volume fraction)

the composite approaches that of the thermal conductivity of the gas phase. In fact, for a steel powder, in a H_2 atmosphere, the experimental value for the effective thermal conductivity in the case of 37% porosity is 2.34 W/(m K) as opposed to 0.52 W/(m K) for a steel (in air) case at low temperatures [103]. As a conclusion, the times for the thermal heat transfer for a sphere (0.5 cm in diameter) is on the order of several seconds.

The times observed in the rearrangement stage during liquid phase sintering in metal systems are higher than those calculated for the approach of particles due to wetting liquid bridges. In contrast, the observed rearrangement times agree with those calculated for heat transfer through a composite powder compact. This indicates that heat transfer is the time limiting factor for rearrangement. Further, the times involved for the approaches of particles (microseconds) agree with the time scales observed for the localized particle regrouping observed *in-situ*. Heat transfer can be considered as a global effect governing the time for rearrangement with the approach of particles due to capillary attraction as a local phenomena. In the above analysis, we treated heat transfer for a composite sphere of 0.5 cm diameter. From Equation 4, the times vary linearly with the compact dimension squared. Therefore, below a specific specimen dimension, the times for rearrangement will be comparable to the times for the approach of particles. In Figures 3.9 and 3.10, we illustrate this phenomena for the W-30Cu and Fe-30Cu systems, respectively. For both cases, in the calculations of the times due to capillary forces, the contact angle is 8°, the particle size ratio is 1 (monosize particles with 1μm particle size) and the liquid volume fraction is 0.1. The lines shown in Figures 6 and 7 represent a dimensional transition between capillary and heat transfer time control. The calculations involved are as follows; The time increments in the radial direction over each liquid bridge for a composite sphere of radius L, are added. The time is then equated to that for heat transfer, Equation 4. The resulting quadratic equation is then solved for the radius L. In this analysis, the effect of porosity is indirectly incorporated through the thermal diffusivities as outlined in Luikov's work [23].

In the above, only metal systems were considered to calculate approximate heat transfer times. For ceramic systems there are two cases to consider: crystalline and amorphous systems as the matrix phase. In the latter case, the matrix does not have a distinct melting point but rather a transition temperature region. In this transition region, the viscosity of the matrix changes orders of magnitude as a function of temperature. Additionally, the viscosities of glasses are much higher than that of metals. This provides a higher viscous drag effect than observed with metal systems. As the viscosity decreases at high temperatures, higher shrinkage or expansion can be observed. Therefore the analysis of Kingery [14] for obtaining a shrinkage dependence on time is fairly correct since it is based on a viscous flow model. However, in the case of crystalline matrix systems, one should consider heat transfer since the matrix has a distinct melting point. Thermal conductivities of oxide ceramics are lower than that of metals. Using the same analysis given in the previous section, times for heat transfer could range up to several minutes. Accordingly heat transfer is considered the time limiting factor for rearrangement.

Since the times for rearrangement are on the order of seconds, experimental control (such as modification of the sintering cycles to enhance densification due to rearrangement) over this stage is difficult. On the other hand, to obtain similar or better mechanical properties than the more traditional heavy alloys, in the W-Ni-Mn system, the solubility of tungsten in the liquid phase and the sintering cycle can be adjusted, to avoid accelerated grain growth.

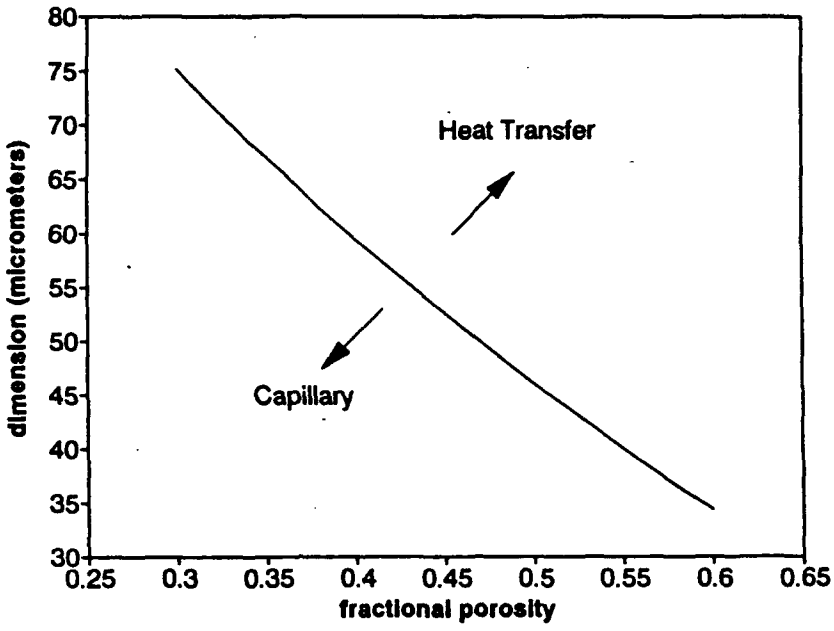

Figure 5. Critical dimension (radius) of a W-30Cu percent by volume composite sphere versus porosity for the transition of the time limiting factor in rearrangement.

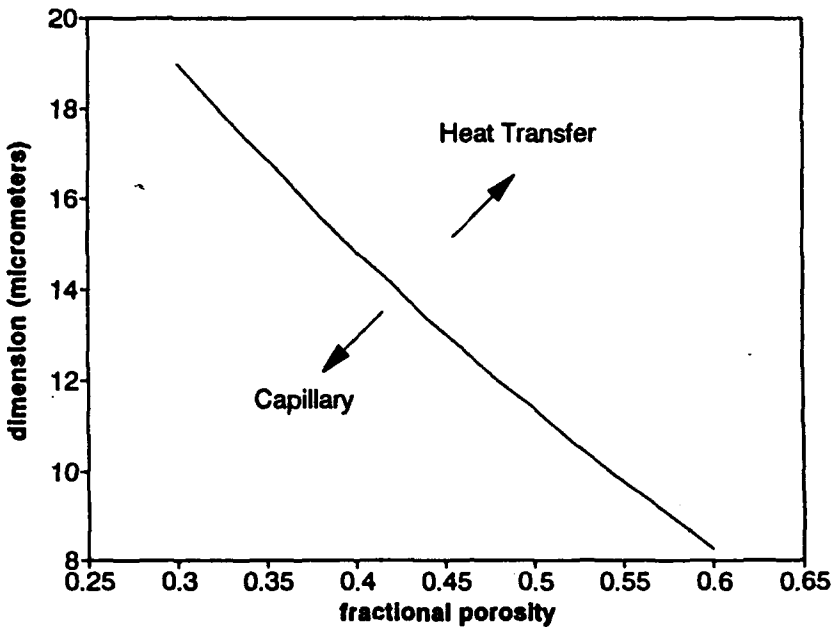

Figure 6. Critical dimension (radius) of a Fe-30Cu percent by volume composite sphere versus porosity for the transition of the time limiting factor in rearrangement.

Grain Growth

The theory of diffusion controlled grain growth from supersaturated solutions has found extensive considerations in the past and present [24-32]. Understanding grain growth enables us to better control microstructures in systems such as liquid phase sintering, precipitate growth in steels and superalloys, and from solutions in chemical processing. Lifshitz and Slyosov [24] concurrent with Wagner [25], hereafter denoted LSW, established a theoretical basis for analyzing the diffusion controlled growth phenomena. Since the number of precipitates or grains in a system is large, grain growth is treated in a continuum basis using statistical analysis. Therefore three considerations are involved when treating grain growth, 1) kinetics of growth, 2) conservation of mass at steady state, and 3) continuity of grain sizes. In the kinetic equation, LSW do not consider the interaction between the diffusion fields around the grains assuming that they interact with a mean field located at infinity [31]. Therefore their analysis is only applicable to an infinitesimal volume fraction of precipitates. From this foundation, different researchers have treated grain growth to include the interactions between the diffusion fields around the grains. Modifications to the LSW analysis can be carried either through the continuity equation to account for coalescence or the kinetic equation to include the interaction of overlapping diffusion fields.

In the present work both approaches were used. In so doing, the Brailsford-Wynblatt analysis [26] for the kinetic equation was adopted since it allows for diffusional interaction between the coarsening grains. A coalescence probability function is then included in grain coarsening. From experimental observations of the coalescence process the following criteria can be deduced,

* TEM analysis of contacting grains revealed that some of them have a liquid film at the contact region and some do not [33],
* In the case of two coalescing grains, both sides of the contact show similar crystallographic orientations [34].
* The amount of coalescing grains is small and ranges from 3 to 5% of the total number of grains [35].

In the tungsten heavy alloy systems, (W-Ni, W-Ni-Fe, W-Ni-Co, W-Ni-Mn), coalescence events are observed. At 1500°C, the tungsten solid-vapor and nickel liquid-vapor surface energies, γ_{SV} and γ_{LV} are respectively 2.62 and 1.85 J/m^2 and the average contact angle θ is between 10 and 20° [36]. assuming that Young's equation is correct, the corresponding average value for the solid-liquid surface energy can be estimated to be 0.8 J/m^2. From the surface energy value calculated above and the average dihedral angle of 25° [37], The resulting average W-W interfacial energy is 1.56 J/m^2. This value is lower than that for the configuration of two grains separated by a liquid indicating that coalescence is favorable in this system. For the Fe-Cu system, the average solid-liquid surface energy is 0.375 J/m^2 as compared to 0.65 J/m^2 for the solid-solid surface energy [38]. Again, coalescence is favored. Moreover, some of the coalescing grains have a thin liquid film between them and some do not. Therefore coalescence appears to be favored by the orientation of grains to form a low energy boundary [33].

Courtney [33] considered the probability for coalescence between two contacting grains, in his treatment, energy-misorientation relationships and geometrical probabilities were used. The probability for coalescence between two grains, P, is found to be dependent on the extent of grain misorientation ϕ, the average solid-liquid surface energy γ and the average solid-solid surface

energy γ_{ss},

$$P = \frac{1}{10}\frac{2\gamma_{SL}}{\gamma_{SS}}\phi\left(1 - \cos\left(\frac{2\gamma_{SL}}{\gamma_{SS}}\phi\right)\right) \qquad (5)$$

The angle ϕ in Equation 5 is reported to have an average value of 12 $\pm$ 5° for a wide variety of materials [33].

Manganese has a high vapor pressure above its melting point. Therefore in the investigation of the coarsening behavior of these alloys, a 90W-4Ni-6Mn composition by weight was considered. This composition was chosen since the liquid formation temperature is the lowest, therefore avoiding Mn loss upon sintering. After mixing and pressing the elemental powders, sintering followed at 1100°C in a H_2 atmosphere for 0, 1, 2, 4, 8, and 16 hours. After sintering, the samples were polished and the grain size was measured using the mean chord intercept method. For the 1, 2, 4, 8, and 16 hours sintering times, the densities were above 95% of theoretical and no major increase in the sintered densities was seen with extended times. This observation insured that above 1 hour sintering time the only sintering event involved was grain coarsening. To identify the mechanism involved in the coarsening of these alloys, the average grain size cubed less G_o^3 is plotted versus time in Figure 7. Regression analysis gave a value of 3.1 for the growth exponent with a growth rate constant K of 2.1×10^{-21} m^3/s. Figure 8 is a plot of the standard deviation of the grain size distribution for each sintering hold versus the decimal logarithm of the ratio of the intercept length and the intercept length at cumulative 50%. As seen in this figure all the grain size distributions exhibit a self similar behavior. The solid line denoted CMDF represents the coalescence modified distribution function, incorporated to the Brailsford and Wynblatt analysis, for a solid volume fraction of 80% (similar to the 90W-6Mn-4Ni by weight composition) and coalescence probability of 3.5% calculated using Equation 5 for the W-Ni system, BW represents the Brailsford and Wynblatt distribution, and 50% represents the CMDF with a coalescence probability of 50%.

The microstructures, of the different sintering times, exhibit spherical grain morphologies typical of tungsten heavy alloys. The grain growth exponent of 3.1, coupled with the tungsten grain shape indicate that the coarsening mechanism is controlled by the diffusion of tungsten through the W-Ni-Mn matrix in contrast with surface controlled growth where the grain growth exponent is usually 2 and the solid grains exhibit faceted shapes as seen in the cemented carbides [7]. Further all the grain size distributions exhibit self similar behavior as shown in Figure 8. This behavior is typical of Ostwald ripening where growth proceeds by the dissolution of the fine grains and growth of the large grains [24]. The self similar behavior arises from the fact that as fine grains dissolve in the matrix and large grains grow the average grain size shifts to a higher value and the same process proceeds again [24,26-28]. The coalescence modified distribution function CMDF shows a good fit with the observed experimental data for the 90W-6Mn-4Ni except at the low and high ends of the distribution. At the low end of the grain size distribution, the CMDF overestimates the probability of finding small grain sizes and at the high end, it underestimates the occurrence of the large grains. Since the grain size effect was not incorporated in the CMDF, this discrepancy arose. In fact, since large grains have high coordination numbers, their probability of coalescence with any other particles increases. For small grains, however, their low coordination number results in a lower coalescence probability. For CMDF distribution with a 50% coalescence probability, it can be seen that the grain size distribution becomes broader

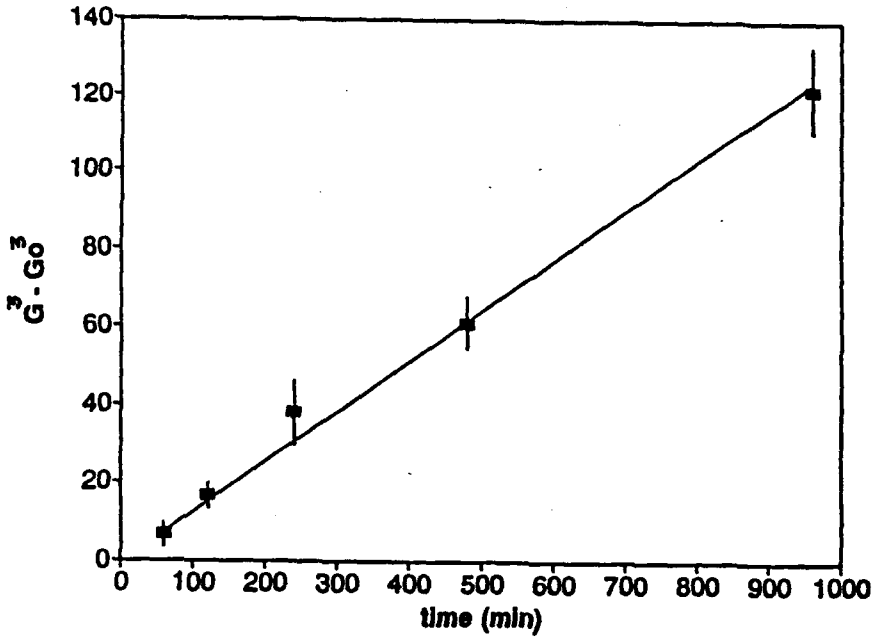

Figure 7. Average intercept length versus time for the 90W-4Ni-6Mn composition sintered at 1100°C in H_2.

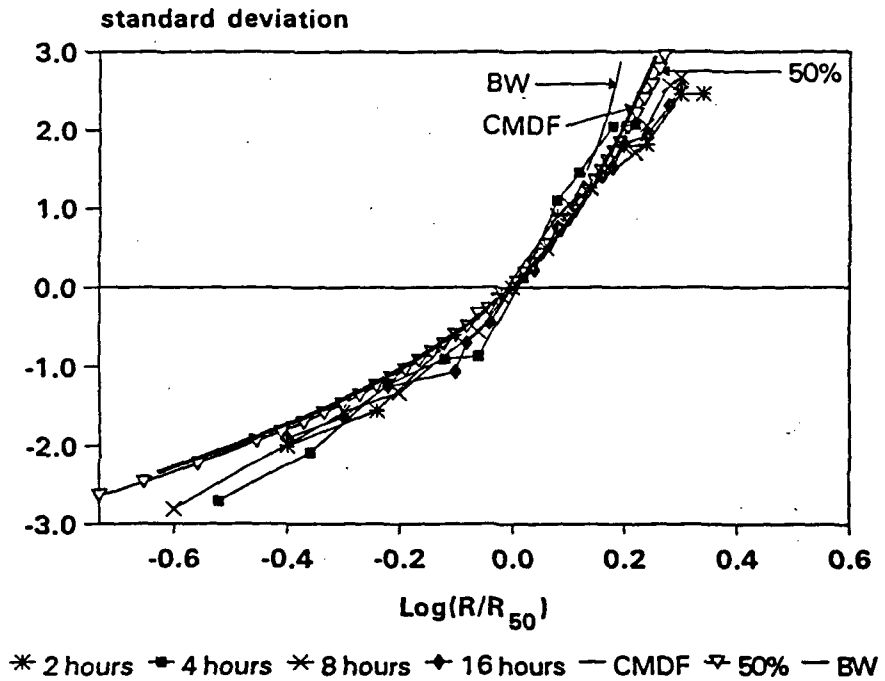

Figure 8. Standard deviation versus the decimal logarithm of the fraction of the grain size to the average intercept length for the 90W-6Mn-4Ni composition sintered at 1100°C in H_2.

coalescence. However, it should be emphasized that the three curves, BW, CMDF at a 3.5% and 50% coalescence probabilities do not show large dissimilarities in the overall behavior of the grain size distribution function. The reason for this behavior is due to the similar grain size dependency on time for diffusion and coalescence controlled grain coarsening [39]. In fact when two particles coalesce, even though their effective volume increases the radii of curvature at each side of the two necking grains is still the same as prior to coalescence. At this point, growth proceeds by a process similar to evaporation-condensation in solid state sintering [39]. However in this case the medium is the liquid matrix rather than the vapor phase. Consequently, diffusion of the solid grain species through the matrix is the time limiting factor for growth by coalescence.

The grain growth exponent of 2.1×10^{-21} m^3/s is well below that observed in 90W-7Ni-3Fe, 1×10^{-18} m^3/s. Since the manganese addition to W-Ni results in a lower solubility of tungsten in the matrix, the grain growth rate is decreased.

In all the proceeding analysis, the tungsten powder used is M-35 and all compositions are given in a weight percent basis unless stated otherwise.

Solubility of W in the Matrix

For the determination of the W solubility in Ni-Mn, elemental W, Ni, and Mn powders with varying Ni/Mn ratios were mixed, pressed, and sintered. For each composition, the tungsten content is kept at 90t%. The sintering temperature for each composition was selected to be 110% of the homologous temperature of the liquid phase with respect to the Ni-Mn binary phase diagram. Sintering consisted of a 10°C/min heating rate then a 1 hour hold followed by water quenching. After metallographic preparation, microprobe analysis was performed. For each specimen six microprobe composition measurements were taken in the matrix. Figure 9 shows the average values for the solubility of tungsten as a function of the Ni/Mn ratio. As illustrated in Figure 9, the tungsten solubility in Ni-Mn decreases as the manganese content increases. This trend is expected since tungsten has no solubility in manganese. Further, nickel and manganese form a complete solid solution (substitutional solid solution), at high ratios of Mn/Ni 4/1 and 1/0, the densification mechanism is expected to shift from solution-reprecipitation to solid-state sintering of the tungsten skeleton as observed in W-Cu systems where tungsten has almost no solubility in Cu [62]. Therefore a highly contiguous microstructure results as shown in Figure 10a. As the Mn to Ni ratio is decreased, the grains show spherical morphology, Figure 10b-c, indicating that solution-reprecipitaion occurred, this effect is further proved through the coarsening behavior in the 90W-6Mn-4Ni system.

Processing of W-Ni-Mn

In the processing of W-Ni-Mn two variables should be considered; 1) The high oxidation potential of manganese and 2) its high vapor pressure above the melting point. These two factors not only affect the microstructure after sintering but also impose an upper bound on the sintering temperature. They further guide the selection of hydrogen as the sintering atmosphere. For example vacuum sintering is not suitable in this system, because there is no kinetic inhibition to manganese evaporation.

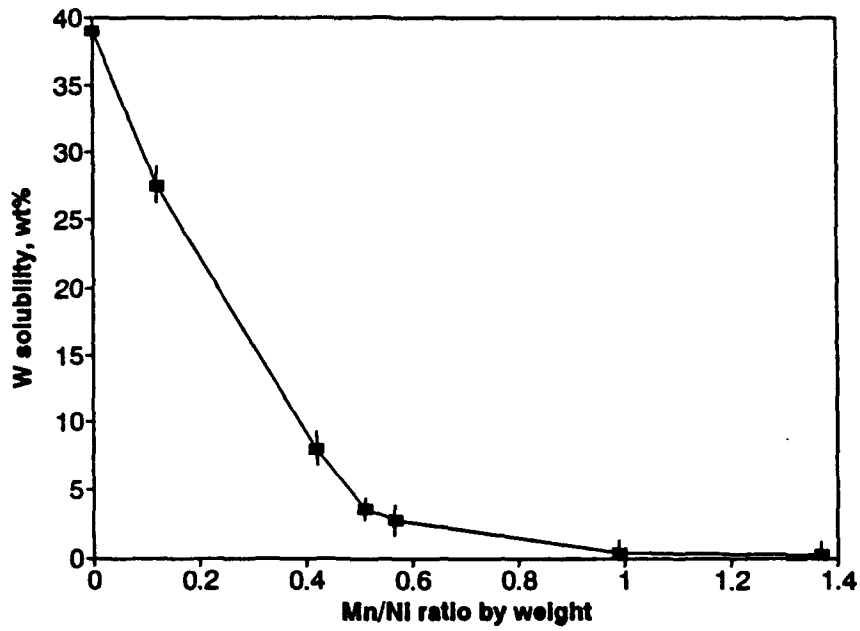

Figure 9. The measured solubility of tungsten as a function of the Ni-Mn ratio, for specimens processed at 110% matrix homologous temperature in hydrogen.

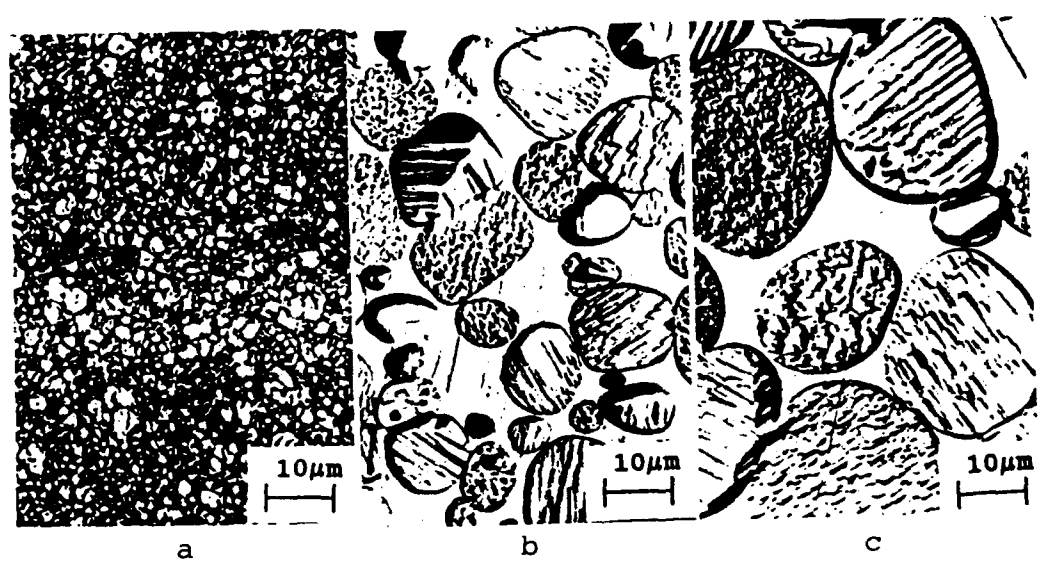

Figure 10. Optical micrographs of 90W with varying Ni/Mn ratios, a) 1/4, b) 3/2, and c) 4/1, sintered at 110% of the matrix homologous temperature.

temperatures. The weight loss is mainly attributed to manganese evaporation due to its high vapor pressure at the sintering temperatures. The weight losses shown in Figure 11 can not be solely attributed to manganese evaporation because two mechanisms can be concurrently occurring; 1. Mn evaporation in the form of the pure element or MnO, 2. Oxide reduction of tungsten and nickel by hydrogen. The oxidation of Mn also proceeds by water vapor and/or oxygen from the environment (W and Ni) and the atmosphere. The evaporating species identified by X-rays are manganese and manganese oxide.

Manganese also has a high oxidation potential. For the oxide reduction of manganese using hydrogen as the processing atmosphere, we consider the following reactions;

$$MnO(s) \rightleftharpoons Mn(s) + \frac{1}{2}O_2(g) \tag{6}$$

$$H_2(g) + \frac{1}{2}O_2(g) \rightleftharpoons H_2O(g) \tag{7}$$

Summing reactions 6 and 7 and their free energies of formations [41] yields,

$$MnO(s) + H_2(g) \rightleftharpoons Mn(s) + H_2O(g) \tag{8}$$

$$\Delta G_T^0 = 138{,}700 - 18\,T(joules/mole) \tag{9}$$

The reaction constant for the equilibrium chemical reaction 8 is given as,

$$K_{eq} = \frac{P_{H_2O}}{P_{H_2}} = \exp\left(\frac{-138{,}700 + 18T}{RT}\right) \tag{10}$$

where R is the gas constant and T is the temperature in K. In the above equations we have assumed that the activities of the solid phases are 1. Figure 12 is a plot of the equilibrium water and hydrogen vapor pressures versus temperature for the chemical reaction 8. Figure 12 shows that even at very dry hydrogen condition (1 ppm), the reduction of manganese oxide is thermodynamically unfavorable. Due to the manganese affinity for oxygen, a high Ni/Mn ratio should be considered to achieve high densification with low oxide contamination of the microstructure.

From Table 1 we single out two compositions promising for full densification, the 3/2 and 4/1 nickel to manganese ratios. Upon tungsten reduction prior to mixing of the 90W-6Ni-4Mn composition, the fractional density has increased from 97.7% for the untreated powders to 98.3% of theoretical, the resulting microstructure is shown in Figure 13. Therefore better control over the hydrogen purity and a low oxygen content in the powders prior to sintering is a must for full densification in these alloys. From oxidation, high manganese vapor pressure, and sintered density criteria, Ni/Mn ratios of 1/4 and 2/3 are eliminated. However, from sintering temperature considerations the 90W-6Ni-4Mn composition (i.e. Ni/Mn ratio of 3/2) is favorable

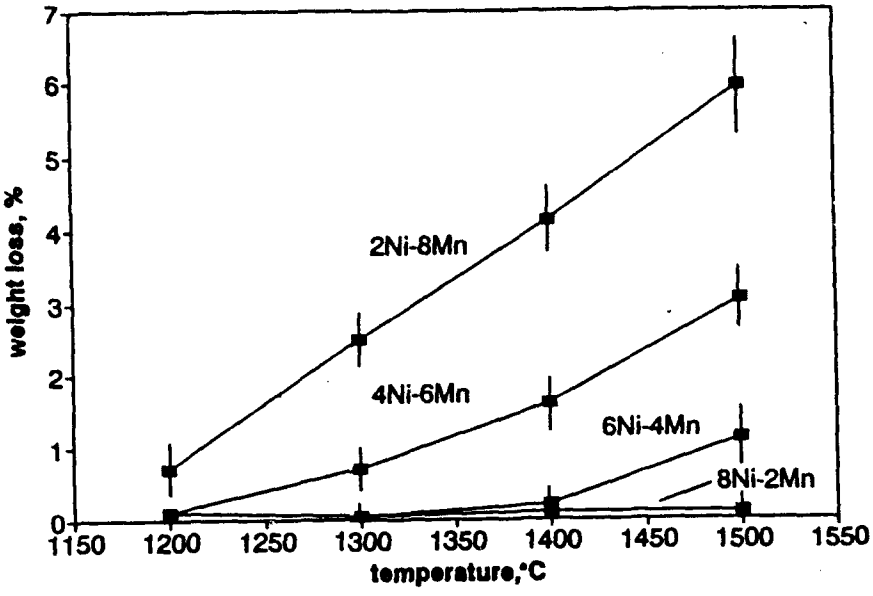

Figure 11. The weight loss versus sintering temperature for a 90W with varying Ni/Mn ratios, 1 hour sintered in a H_2 atmosphere, for cylindrical samples of 12.74 mm diameter and around 8 mm height.

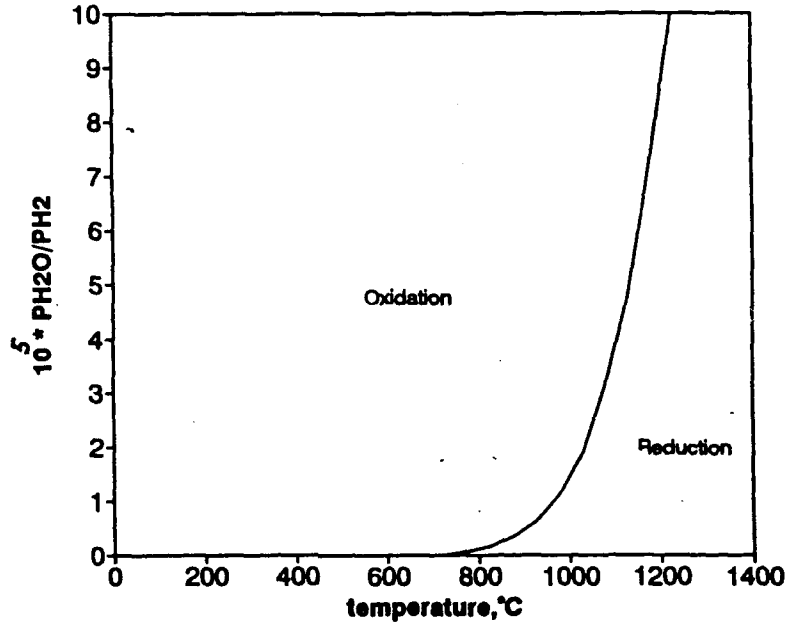

Figure 12. The equilibrium water and hydrogen vapor pressures versus temperature for the oxidation-reduction of pure manganese.

higher for the latter composition. Further, the mechanical properties (presented in the next section) of the Ni/Mn with a composition ratio of 3/2 are superior to that of the 4/1 ratio. From the above considerations, we select the 3/2 nickel to manganese ratio as an optimum matrix composition to achieve high densifications concurrent with high mechanical performance.

Mechanical Properties

For the evaluation of the mechanical properties in the W-Ni-Mn system, the compositions tensile tested were 90W-8Ni-2Mn sintered at 1300 and 1400°C for 1 hour, 90W-6Ni-4Mn, 85W-9Ni-6Mn, and 80W-12Ni-8Mn sintered at 1200°C for 1 hour H_2.

During tensile testing, the as-sintered specimens showed no ductility and failed at the grips. Figure 14 shows characteristic fracture surfaces in this system. As shown in this figure, the tungsten grains exhibit no cleavage. In fact brittle failure has occurred at the matrix-tungsten grains interface. This is evident from the matrix pull-out shown in the above figure. Hydrogen embrittlement can also play a role in the degraded properties of these specimens. To single out the role of hydrogen, specimens of 90W-6Ni-4Mn are heat treated in argon at 1100°C, 1000°C, and 900°C for 1 hour and furnace cooled. The argon treatment ensures that hydrogen degassing occurred. These samples still failed prematurely. The premature failure of the as sintered specimens can be traced back to the nickel-manganese binary phase diagram, Figure 1. As shown in this figure, there is a large field of intermetallics under the solidus curve. Therefore during cooling from the sintering temperature, the microstructure undergoes phase changes according to the phase diagram and intermetallics form. Intermetallic formation in the matrix is detrimental to the mechanical properties [40-44]. Another embritteling phase usually observed in the processing of W-Ni and W-Ni-Fe is the Ni_4W intermetallic. This phase persists at temperatures below 970°C during cooling from the sintering temperature. As a consequence fracture occurs at the W-matrix interface preventing any tungsten cleavage.

After sintering, specimens of the 90W-6Ni-4Mn composition were quenched from 950, 1000, and 1050°C in a water bath. The heat treatment atmosphere used is argon. The quenching temperature was selected so that the microstructure is in a field where no intermetallic formation occurs and below the liquidus formation temperature shown in Figure 1. The 950°C quenching

temperature was chosen to test if in the W-Ni-Mn ternary system the Ni_4W phase (occurring below 970°C) contributes to the degradation of these alloys. For the above quenching temperatures the resulting ultimate tensile strength was 900 MPa with a 10% elongation to failure. Figure 15 is a typical SEM micrograph of fracture surfaces for the water quenched specimens. The tungsten grains in this case show cleavage and the matrix shows ductile behavior.

In the above experiments, prior to sintering, the initial powder mixtures were not milled. The resulting mechanical properties are given in Table 2. As shown in this table, the specimens exhibit ductility and high strength values. Tensile specimens were also made from planetary milled powders for 1 hour with different compositions: 90W-6Ni-4Mn, 85W-9Ni-6Mn, and 80W-12Ni-8Mn. The sintering cycle consists of a 10°C/min ramp to 1200°C followed by a 1 hour hold in H_2. The heat treatment cycle proceeded at 1000°C for 1 hour followed by quenching in a water bath. The mechanical properties are given in Table 3. As shown in this table, higher strength are observed with a 980 MPa UTS as compared to 900 MPa for the unmilled powders.

Table 1. Density (% theoretical) as a function of sintering temperature in the W-Ni-Mn system.

Temperature (°C)	90W-8Ni-2Mn	90W-6Ni-4Mn	90W-4Ni-6Mn
1200	86.6	97.7	95.9
1300	98.6	97.3	95.4
1400	97.7	97.3	96.8
1500	97.4	97.8	96.2

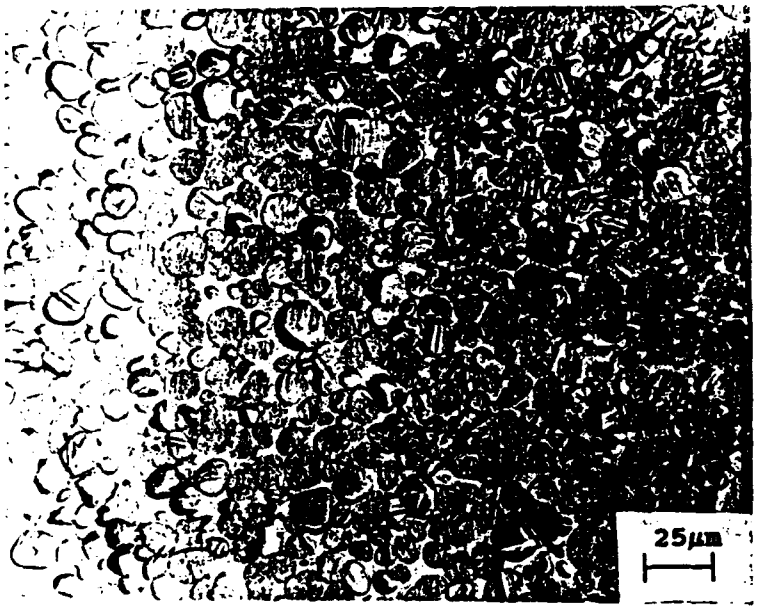

Figure 13. Optical micrograph of the microstructure of 90W-6Ni-4Mn sintered at 1200°C for 1 hour in H_2.

In accordance with the post-sintering cycle, the mechanical properties have improved. However, for the three quenching cycles, the ductility and ultimate tensile strength were not affected by the quenching temperature variations. In this temperature region, intermetallic formation in the Ni-Mn system is avoided. For the specimens quenched from 1000°C and 1050°C, the Ni_4W phase should be avoided. However, the specimens quenched from the 950°C temperature do not show lower ductilities than the ones treated at the higher temperatures. This is probably due to the low Ni/Mn (3/2) ratio used in this study as compared to W-Ni-Fe where high Ni/Fe ratios are used (7/3 to 4/1), which favor the formation of this brittle phase. The effect of the Ni_4W intermetallic phase is more evident in the 90W-8Mn-2Ni compositions (Ni to Mn ratio is 4/1) sintered at 1400°C and post- sintering heat treated using the above quenching cycles. In this case, the percent elongation to failure is around 4% with a UTS of 890 MPa. To further optimize the heat treatment cycle, more work is needed to determine the occurrence of intermetallic phases in the W-Ni-Mn system as no W-Mn phase diagram currently available.

The strength values increase with increasing tungsten content, as shown in Table 3, is expected in tungsten heavy alloys. However the ductility is the same for different matrix weight fraction considered indicating that it is more sensitive to the porosity associated with oxide formation than to the matrix volume fraction. Nevertheless, the mechanical properties observed in this system are encouraging given that the densities achieved are only around 98% of theoretical. Further studies to achieve full densification in this system are needed. A feasible approach is the use of prealloyed powders to lower the oxidation associated with elemental manganese powders.

Figure 14. Typical fracture surface microstructure of as sintered 90W-6Ni-4Mn.

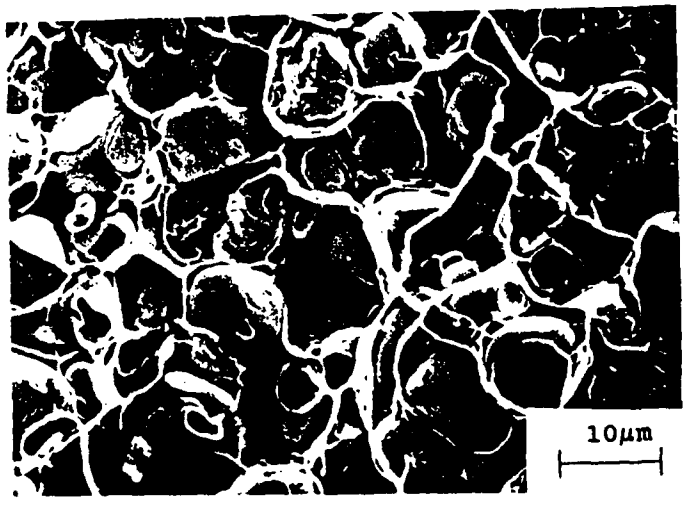

Figure 15. Fracture surface of water quenched 90W-6Ni-4Mn.

Table 2. Heat treatment effects on the mechanical properties of W-Ni-Mn.

Heat treatment	UTS (MPa)	% Elongation
As-sintered*	Broke at the grips	Brittle behavior
Quenching from 950°C **	895 ± 10	10 ± 1
Quenching from 1000°C **	900 ± 15	9.5 ± 0.8
Quenching from 1050°C **	902 ± 12	9.4 ± 0.7
Quenching from 1050°C ***	895 ± 10	4 ± 0.8

* all Ni/Mn ratios
** 90W-6Ni-4Mn
*** 90W-8Ni-2Mn

Table 3. Mechanical properties of W-Ni-Mn, 1 hour planetary milled powders.

Composition	UTS (MPa)	% Elongation
90W-6Ni-4Mn	980 ± 10	10 ± 1
85W-9Ni-6Mn	910 ± 15	9.6 ± 0.6
80W-12Ni-8Mn	880 ± 10	10 ± 1

Summary

In the selection of a new heavy alloy for low temperature sintering, the solubility of tungsten in the matrix, wetting of the solid phase by the liquid, capillary induced rearrangement, grain coarsening, processing, and the mechanical properties of W-Ni-Mn were investigated.

When criteria such as the wetting angle, the volume fraction and viscosity of the liquid phase, and the solid phase grain size were incorporated in a treatment of the capillary induced rearrangement, four observations are deduced, 1) a broad particle size distribution and a homogenous distribution of the liquid phase enhance densification, 2) the times involved in the shrinkage (or swelling), when capillary and viscous drag forces are considered, are on the order of microseconds, 3) heat transfer is the time limiting factor for the shrinkage during rearrangement, and 4) in cases where the matrix phase is not crystalline, viscous drag becomes important and therefore slows the approach of the particles due to capillary forces. In such a case, the shrinkage-time dependence developed by Kingery is applicable.

While good wetting of tungsten by the liquid phase results in high densifications through rearrangement, full densification is achieved when solution-reprecipitation occurs. To enhance densification beyond the rearrangement stage, the solubility of the solid phase in the liquid is a requirement. Therefore in the development of a tungsten heavy alloy, the presence of a liquid phase that provides solubility for tungsten, such as nickel, is beneficial. However, enhanced solution-reprecipitaion also results in accelerated grain growth which is not desirable with respect to the mechanical properties of the composite. To control grain growth, manganese is added to the W-Ni system. The resulting growth rate constant for 90W-6Mn-4Ni sintered at 1100°C was 2.1×10^{-21} m^3/s which is well below that observed in 90W-7Ni-3Fe, 1×10^{-18} m^3/s sintered at 1500°C. The decrease in the growth rate constant is due to the lack of solubility of tungsten in manganese. Nevertheless, the growth kinetics in the W-Ni-Mn system during liquid phase sintering was diffusion controlled as previously observed in tungsten heavy alloys. During this stage, coalescence also contributes to coarsening. When coalescence was incorporated into the coarsening problem, three results were found in agreement with experimental observations, 1) broadening of the grain size distribution function, 2) the distribution function became more symmetrical and skewed to the right at the high volume fractions, and 3) the growth rate constant increased. In this treatment the effect of the coordination number of grains surrounding a specific grain size was not included in the coalescence function. This resulted in a discrepancy between the theoretical treatment and the experimental observations at both ends of the grain size distribution. To allow for this effect, the number of contacts as a function of the grain size and the volume fraction of the coarsening phase needs to be considered. Nevertheless, it was found that the overall effect of coalescence on the grain size distribution functions was not as significant as previously thought.

The effect of manganese on the W-Ni system results in a depressed melting point of the matrix, allowing densification to proceed at temperatures 300°C lower than commonly used in the conventional heavy alloys. However, due to the high vapor pressure and oxidation potential of manganese, three criteria need to be followed to achieve high densifications upon sintering W-Ni-Mn, 1) the initial amounts of oxides in the original powders should be low (for example the initial tungsten powders can be reduced at 800°C in a hydrogen atmosphere), 2) sintering at low temperatures, and 3) a high Ni/Mn ratio is desirable. The optimum Ni to Mn ratio, with respect to density, sintering temperature, and mechanical properties, was found to be 3/2 with a sintering

temperature around 1200°C.

The as-sintered W-Ni-Mn composites failed in the elastic region during tensile testing due to Ni-Mn intermetallic formation after sintering. In accordance with the Ni-Mn phase diagram, a post-sintering heat treatment at 1000°C followed by water quenching resulted in a 900 MPa ultimate tensile strength and 10% ductility. This heat treatment cycle was designed to avoid intermetallic formation in the matrix. The pore morphology in this system was similar to the initial manganese powder shape. In fact, milling of the initial powders resulted in a smaller pore size and higher mechanical properties, 980 MPa and 10% ductility for the 90W-6Ni-4Mn composition.

In accordance with phase relationships, solubility criteria, wetting, grain growth kinetics, and optimized processing conditions, we have successfully developed a new tungsten heavy alloy, W-Ni-Mn. This novel heavy alloy is competitive to the more traditional heavy alloys considering that the sintering temperature is lowered by 300°C and the mechanical properties are comparable.

Publications

T. Kishi and R. M. German, "Processing Effects on the Mechanical Properties of Tungsten Heavy Alloys," International Journal of Refractory Metals and Hard Materials, 1990, vol. 9, pp. 40-45.

S. C. Yang, S. S. Mani and R. M. German, "The Effect of Contiguity on Growth Kinetics in Liquid Phase Sintering," Journal of Metals, 1990, vol. 42, no. 5, pp. 16-19.

A. Bose and R. M. German, "Matrix Composition Effects on the Tensile Properties of Tungsten-Molybdenum Heavy Alloys," Metallurgical Transactions, 1990, vol. 21A, pp. 1325-1327.

S. C. Yang, S. S. Mani and R. M. German, "Grain Growth Behavior in Liquid Phase Sintered Heavy Alloys," Advances in Powder Metallurgy, vol. 1, E. R. Andreotti and P. J. McGeehan (eds.), Metal Powder Industries Federation, Princeton, NJ, 1990, pp. 469-482.

A. Bose, H. Zhang, P. Kemp and R. M. German, "Injection Molding of Molybdenum Treated Tungsten Heavy Alloy," Advances in Powder Metallurgy, vol. 3, E. R. Andreotti and P. J. McGeehan (eds.), Metal Powder Industries Federation, Princeton, NJ, 1990, pp. 401-413.

A. Belhadjhamida and R. M. German, "Tungsten and Tungsten Alloys by Powder Metallurgy: A Status Review," Tungsten and Tungsten Alloys, A. Crowson and E. S. Chen (eds.), The Minerals, Metals and Materials Society, Warrendale, PA, 1991, pp. 3-18.

R. M. German and A. Bose, "Properties of High Density Tungsten-Rhenium Alloys by Liquid Phase Sintering," Tungsten and Tungsten Alloys, A. Crowson and E. S. Chen (eds.), The Minerals, Metals and Materials Society, Warrendale, PA, 1991, pp. 53-59.

J. Lankford, H. Couque, A. Bose and R. M. German, "Dynamic Deformation and Failure of Tungsten Heavy Alloys," Tungsten and Tungsten Alloys, A. Crowson and E. S. Chen (eds.), The Minerals, Metals and Materials Society, Warrendale, PA, 1991, pp. 151-159.

R. M. German, "Limitations in Net Shaping by Liquid Phase Sintering," Advances in Powder Metallurgy -1991, vol. 4, L. F. Pease and R. J. Sansoucy (eds.), Metal Powder Industries Federation, Princeton, NJ, 1991, pp. 183-194.

A. Bose, S. C. Yang and R. M. German, "Development of a New W-Ni-Mn Heavy Alloy," Advances in Powder Metallurgy -1991, vol. 6, L. F. Pease and R. J. Sansoucy (eds.), Metal Powder Industries Federation, Princeton, NJ, 1991, pp. 425-437.

A. Belhadjhamida and R. M. German, "The Effects of Powder Pretreatment on the Microstructure and Mechanical Properties of Tungsten Heavy Alloys," Advances in Powder Metallurgy - 1991, vol. 6, L. F. Pease and R. J. Sansoucy (eds.), Metal Powder Industries Federation, Princeton, NJ, 1991, pp. 407- 423.

S. C. Yang and R. M. German, "Generic Grain Size Distribution for Liquid Phase Sintering," Scripta Metallurgica et Materialia, 1992, vol. 26, pp. 95-98.

R. M. German, A. Bose and S. S. Mani, "Sintering Time and Atmosphere Influences on the Microstructure and Mechanical Properties of Tungsten Heavy Alloys," Metallurgical Transactions, 1992, vol. 23A, pp. 211-219.

R. M. German, "Microstructural Evolution in Liquid Phase Sintering," Sintering '91, A. C. D. Chaklader and J. A. Lund (eds.), Proceedings of the Fifth International Symposium on the Science and Technology of Sintering, Trans Tech Pub., Brookfield, VT, 1992, pp. 73-87.

A. Belhadjhamida and R. M. German, "The Effects of Atmosphere, Temperature, and Composition on the Densification and Properties of Tungsten-Nickel-Manganese," Advances in Powder Metallurgy and Particulate Materials, vol. 3, J. M. Capus and R. M. German (eds.), Metal Powder Industries Federation, Princeton, NJ, 1992, pp. 47-55.

R. M. German, "Critical Developments in Tungsten Heavy Alloys," Tungsten and Tungsten Alloys - 1992, A. Bose and R. J. Dowding (eds.), Metal Powder Industries Federation, Princeton, NJ, 1993, pp. 3-13.

G. Harshe, V. Srikanth and R. M. German, "A New Family of Hard Materials: W-Ni-Fe-B_4C," Tungsten and Tungsten Alloys - 1992, A. Bose and R. J. Dowding (eds.), Metal Powder Industries Federation, Princeton, NJ, 1993, pp. 35-42.

A. Belhadjhamida and R. M. German, "Heat Treatment and matrix Volume Fraction Effects on the Mechanical Properties of Tungsten-Nickel-Manganese," Tungsten and Tungsten Alloys - 1992, A. Bose and R. J. Dowding (eds.), Metal Powder Industries Federation, Princeton, NJ, 1993, pp. 195-204.

V. Srikanth, G. Harshe and R. M. German, "Effect of Molybdenum Addition to W-Ni-Fe-B_4C Nonconventional Hard Materials," Tungsten and Tungsten Alloys - 1992, A. Bose and R. J. Dowding (eds.), Metal Powder Industries Federation, Princeton, NJ, 1993, pp. 205-212.

Advanced Degrees Earned

Abdelhakim Belhadjhamida earned a PhD in Engineering Science and Mechanics.

References

1. C.J. Smithells, *Tungsten: A Treatise on its Metallurgy, Properties, and Applications*, D. Van Norstrand Company N.Y, (1927), 1.

2. W.D. Coolidge, "Ductile Tungsten," *Trans A.I.E.E*, 29(1910), 961-965.

3. W.D. Jones, *Fundamental Principles of Powder Metallurgy*, London, Edward Arnold Publishers, (1960), 600.

4. C.J. Smithells, W.R. Pitkins, and J.W. Avery, "Grain Growth in Compressed Metal Powder," *J. Inst. Metals*, 38(1927), 88-102.

5. G.H. S. Price, C.J. Smithells, and S.V. Williams, "Copper-Nickel-Tungsten Alloys Sintered with a Liquid Phase Present," *J. Inst. Metals*, 62(1938), 239-264.

6. F.V. Lenel, *Powder Metallurgy Principles and Applications*, Metal Powder Industry Federation, Princeton, NJ, (1980), 337-348.

7. R.M. German, *Liquid Phase Sintering*, Plenum Press, NY, (1985).

8. C.G. Goetzel, *Treatise on Powder Metallurgy*, New York, NY: Interscience, 1(1949), 534-536.

9. E.I. Larson, P.C. Murphy, "Characteristic and Applications of High-Density Tungsten-Based Composites," *Can. Min. Met. Bull.*, (1965), 413-420.

10. H.G. Sell, *Refractory Metal Alloys*, Edited by I. Machlin, R.T. Begley, and E.D. Weisert, Plenum Press, NY, (1968), 395-439.

11. W.D. Jones, *Fundamental Principles of Powder Metallurgy*, London, Edward Arnold Publishers, (1960), 53-56.

12. A. Bose, D.M. Sims, and R.M. German," High Strength Tungsten Heavy Alloys with Molybdenum Additions," *Prog. Powder Met.*, 43(1987), 79-92.

13. T.B. Massalski (ed), Binary Alloy Phase Diagrams, *Am. Soc. Met.*, Metal Park, OH, (1986).

14. W.D. Kingery, "Densification During Sintering in The Presence of a Liquid Phase 1. Theory," *J. Appl. Phys.*, 30(1959), 301-306.

15. W.J. Huppman, H. Riegger, W.A Kaysser, V. Smolej, and S. Pejovnik, "The Elementary Mechanism of Liquid Phase Sintering I. Rearrangement," *Z. Metallkde.*, 70(1979), 707-713.

16. J.W. Cahn and R.B. Heady, "Analysis of Capillary Forces in Liquid Phase Sintering of

Spherical Particles," *Met. Trans.*, 1(1970), 185-189.

17. J.W. Cahn and R.B. Heady, "Analysis of Capillary Forces in Liquid-Phase Sintering of Jagged Particles," *J. Am. Cer. Soc.*, 53(1970), 406-409.

18. M.A. Fortees, "The Kinetics of Powder Densification Due to Capillary Forces," *Powder Met. Inter.*, 14(1982), 96-100.

19. L. Froshauer and R.M. Fulrath, "Direct Observation of Liquid Phase Sintering in the System Iron-Copper," *J. Mat. Science.*, 10(1975), 2146-2155.

20. L. Froshauer and R.M. Fulrath, "Direct Observation of Liquid Phase Sintering in the System Tungsten Carbide-Cobalt," *J. Mat. Science.*, 11(1976), 142-149.

21. K.S. Hwang, R.M. German, and F.V. lenel, "Capillary Forces between Spheres during Agglomeration and Liquid Phase Sintering," *Met. Trans.*, 18A(1987), 11-17.

22. J.C. Melrose, "Model Calculations for Capillary Condensation," *J. A.I.Ch.E.*, 12(1966), 986-994.

23 A.V. Luikov, A.G. Shashkov, L.L. Vasiliev, and Y.E. Fraiman, "Thermal Conductivity of Porous Systems," *Int. J. Heat Mass Transfer*, 11(1968), 117-140.

24. I.M. Lifshitz and V.V. Slyozov, "The Kinetics of Precipitation From Supersaturated Solid Solutions," *J. Phys, Chem. Solids*, 19(1961), 35-50.

25. C. Wagner," Theorie der Alterung von Niederschlagen durch Umlosen," *Z. Elecrochem.*, 65(1961), 581-591.

26. A.D. Brailsford and P. Wynblatt, "The Dependance of Ostwald Ripening Kinetics on Particle Volume Fraction," *Acta. Met.*, 27(1979), 489-497.

27. C.K. L. Davis, P. Nash, and R.N. Stevens, "The Effect of Volume Fraction of Precipitate on Ostwald Ripening," *Acta. Met.*, 38(1980), 179-189.

28. P.W. Voorhees and M.E. Glicksman, "Ostwald Ripening During Liquid Phase Sintering-Effect of Volume Fraction on Coarsening Kinetics," *Met. Trans. A.*, 15A(1984), 1081-1088.

29. A.J. Ardell, "The Effect of Volume fraction on Particle Coarsening: Theoretical Considerations," *Acta. Met.*, 20(1972), 61-71.

30. J.J. Weins and J.W. Cahn, "The effect of Size and Distribution of Second Phase Particles and Voids On Sintering" *in Sintering and Related Phenomena*, G.C Kuczynsky, (ed.), Plenum Press. London. 1973, 151-163.

31. T.H. Courtney, "Microstructural Evolution During Liquid Phase Sintering: Part II.

Microstructural Coarsening," *Met. Trans.*, **8A**(1977), 685-689.

32. P.W. Voorhees, "The Theory of Ostwald Ripening," *J. Stat. Phys.*, **38**(1985), 231-252.

33. T.H. Courtney and J.K. Lee, "An Analysis for Estimating the Probability of Particle Coalescence in Liquid Phase Sintered Systems," *Met. Trans.*, **11A**(1980), 943-947.

34. R.M. German, private communications

35. S.C. Yang and R.M. German, "Grain Growth Kinetics in Liquid-Phase-Sintered Zinc Oxide-Barium Oxide Ceramics," *J. Am. Cer. Soc.*, **74**(1991), 3085-3090.

36. H. Jones, "The Surface Energy of Solid Metals," *J. Met. Sci.*, **5**(1971), 15-18.

37. D.F. Heaney, I.S. Ahn, and R.M. German, private communications.

38. R. Watanabe and Y. Masuda, "The Growth of Solid Particles in Fe-20 wt% Cu Alloy During Sintering in the Presence of a Liquid Phase ", *Trans. JIM.*, **14**(1973), 320-326.

39. T.H. Courtney, "A Reanalysis of the Kinetics of Neck Growth During Liquid Phase Sintering," *Met. Trans.*, **8A**(1977), 671-677.

40. R.M. German and K.S. Churn, "Sintering Atmosphere Effects on the Ductility of W-Ni-Fe Heavy Metals," *Met. Trans. A.*, **15A**(1984), 747-754.

41. W.E. Gurwell, "A Review of Embrittlement Mechanisms in Tungsten Heavy Alloys," *Report PNL-SA-13645*, Pacific Northwest Laboratory, Richland, WA, April 1986.

42. B.H. Rabin and R.M. German, "Microstructure Effects on Tensile Properties of Tungsten-Nickel-Iron," *Met. Trans. A.*, **19**(1988), 1523-1532

43. T. Kaneko, "Effect of Microstructure on the Mechanical Properties of Sintered Tungsten Base Alloys," *J. Japan Soc. Powder Met.*, **37**(1990), 885-892.

44. R.M. German, J.E. Hanafee, and S.L. DiGiallonardo, "Toughness Variation with Test Temperature and Cooling Rate for Liquid Phase Sintered W-3.5Ni-1.5Fe," *Met. Trans. A*, **15A**(1984), 121-128.